Sensing the Local Magnetic Environment through Optically Active Defects in a Layered Magnetic Semiconductor

Julian Klein,* Zhigang Song, Benjamin Pingault, Florian Dirnberger, Hang Chi, Jonathan B. Curtis, Rami Dana, Rezlind Bushati, Jiamin Quan, Lukas Dekanovsky, Zdenek Sofer, Andrea Alù, Vinod M. Menon, Jagadeesh S. Moodera, Marko Lončar, Prineha Narang,* and Frances M. Ross*

ACCESS | Metrics & More | Article Recommendations | SI Supporting Information

ABSTRACT: Atomic-level defects in van der Waals (vdW) materials are essential building blocks for quantum technologies and quantum sensing applications. The layered magnetic semiconductor CrSBr is an outstanding candidate for exploring optically active defects because of a direct gap, in addition to a rich magnetic phase diagram, including a recently hypothesized defect-induced magnetic order at low temperature. Here, we show optically active defects in CrSBr that are probes of the local magnetic environment. We observe a spectrally narrow (1 meV) defect emission in CrSBr that is correlated with both the bulk magnetic order and an additional low-temperature, defect-induced magnetic order. We elucidate the origin of this magnetic order in the context of local and nonlocal exchange coupling effects. Our work establishes vdW magnets like CrSBr as an exceptional platform to optically study defects that are correlated with the magnetic lattice. We anticipate that controlled defect creation allows for tailor-made complex magnetic textures and phases with direct optical access.

KEYWORDS: *CrSBr, van der Waals magnet, defect emission, defect magnetic order, magnetic correlation, magnetic semiconductor, sensing*

Spin defects in solids make up a vastly growing field, both fundamental and applied, and play an important role in emergent quantum technologies.[1−8] While single isolated defects in a solid are practical for the emission of nonclassical light or applications in quantum sensing,[2,9] closely arranged spin defects provide a means to explore complex quantum many-body systems in the solid state,[10] similar to trapped atomic or ionic systems.[11] Such systems are of key interest for quantum simulation of spin-Hamiltonians for exploring exotic properties in solid-state materials.[12−16] In terms of local creation of defects with functional properties, the class of two-dimensional (2D) materials offers advantages over conventional three-dimensional (3D) materials.[17] Several optically active defects in 2D materials have been identified[18] and also deterministically positioned[19,20] with the motivation to provide a platform for scalable single-photon sources.[21−23] 2D magnets offer opportunities for using defects for designing artificial magnetic orders or magnetic quasiparticles like magnetic vortices (e.g., skyrmions) for applications in nanospintronics and quantum memories.[24] As of yet, optically
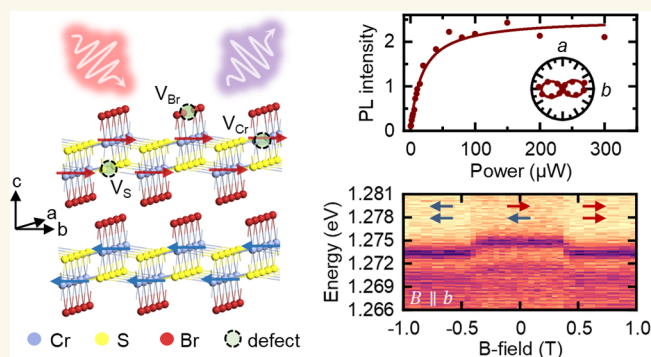
active defects in 2D magnets have been scarcely explored,[25] often because of material instability, the absence of a band gap, or poor optical emission properties[26,27] and therefore, have been mostly limited to theoretical work.[24]

The layered magnetic semiconductor CrSBr is a promising van der Waals (vdW) material ideal for pursuing 2D magnetism[28−30] because of its good air stability, sizable band gap ~1.5 eV,[31] high transition temperature (132 K) with A-type antiferromagnetic (AFM) order,[31] tightly bound magneto-excitons,[32] and correlated magneto-transport.[33] Moreover, the charge transport is highly anisotropic[34] even in multilayer CrSBr flakes, whose origin is a strong one-dimensional (1D) electronic character because of an intricate combination of
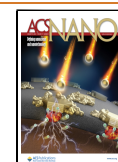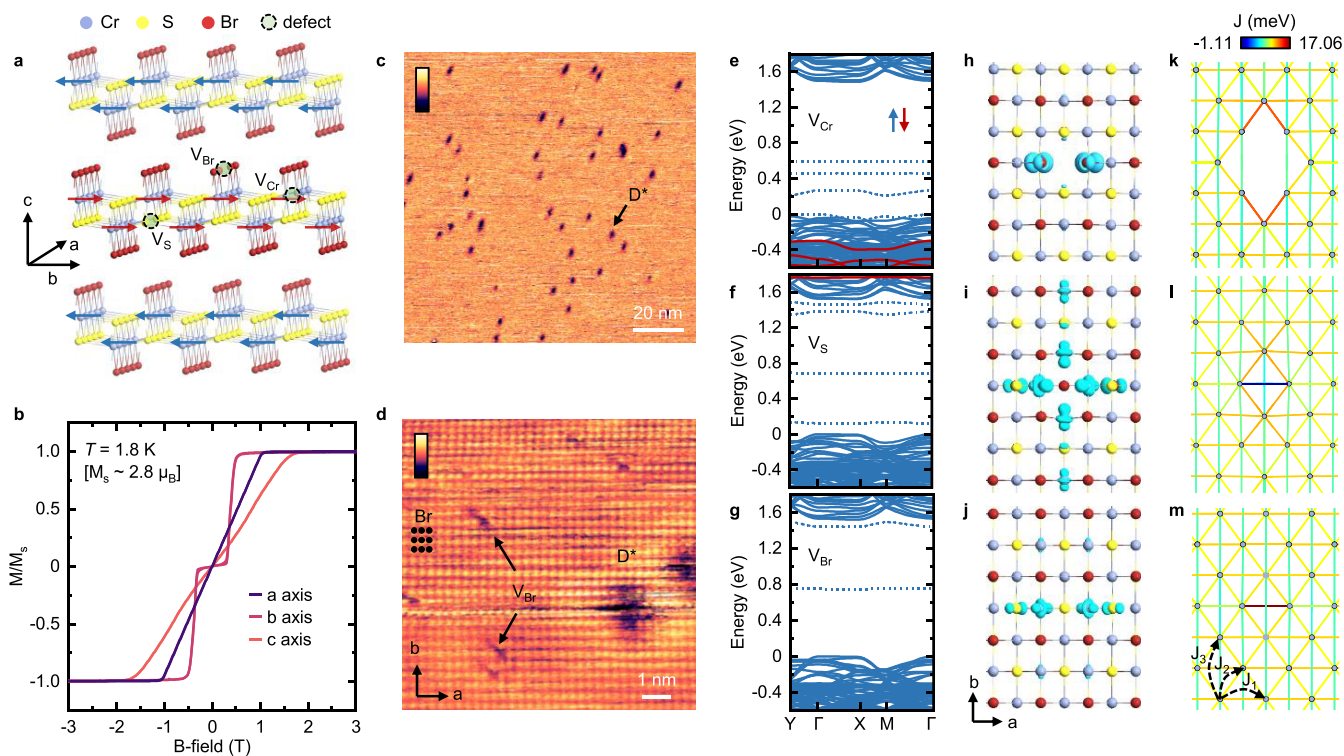
Figure 1. Intrinsic crystal defects in CrSBr and their calculated electronic and magnetic properties. (a) Schematic illustration of multilayer CrSBr with moment indicated in each layer and point vacancy defects within one layer. (b) Magnetization at 1.8 K measured with the magnetic field oriented along the a, b, and c axes. The magnetization saturates at 2.8 μ_B close to the $S = +3/2$ for ferromagnetic interlayer coupling. (c) Large-area room temperature STM topographic image of the surface defect concentration of at least one defect with a low density of $\sim 3 \times 10^{11}$ cm^{-2}. Tunneling current of 20 pA and a bias voltage of 0.4 V. (d) High magnification STM topographic image shows the top layer of Br atoms and individual Br vacancy point defect with a surface density of $\sim 5 \times 10^{12}$ cm^{-2} (sheet density of $\sim 10^{13}$ cm^{-2}). (e) Ab initio calculated electronic band structure using the Heyd–Scuseria–Ernzerhof (HSE) functional of the V_{Cr}, (f) V_S, and (g) V_{Br} for a $7 \times 7 \times 1$ supercell. (h) Top view of the calculated real-space wave functions of V_{Cr}, (i) V_S, and (j) V_{Br}. (k) Calculated Heisenberg exchange interaction J in the presence of V_{Cr}, (l) V_S, and (m) V_{Br}.

weak interlayer hybridization and strong intralayer anisotropic electronic band structure.[35] This has the advantage that optically clean signatures and magnetic orderings that mimic mono- or bilayer CrSBr can be conveniently probed in disorder-free, high-quality multilayer crystals.[35]

The magnetic phase diagram of CrSBr is rich and displays a low-temperature magnetic order that emerges at a critical temperature of $T_D = 30–40$ K.[31,33,36,37] This magnetic order has been observed consistently in magnetic susceptibility and magneto-transport measurements throughout all reported crystals. The origin of this magnetic signature is still under debate, but has been speculated to arise from crystal defects.[33,36,37] The defect exchange coupling and defect-to-defect exchange interactions are, therefore, likely to play an important role in the formation of this magnetic order but are as of yet unknown. Indeed, the type and density of intrinsic defects in CrSBr and their electronic, optical, and magnetic properties are mostly unexplored. The strong optical response of this material,[32] in particular its very narrow spectral width in multilayer crystals,[35] therefore creates a powerful motivation to study whether optically active defects are present in CrSBr, their sensitivity to the magnetic order, and their role in the emergence of the low-temperature magnetic order at $T_D = 30–40$ K. This will be crucial in exploiting crystal defects for applications in magnetic sensing and for creating exotic many-body states.

Here, we show that CrSBr does, indeed, host optically active defect states that are correlated with the magnetic phase diagram. We quantify the intrinsic defects in CrSBr by scanning tunneling microscopy (STM) and observe that the most abundant defect is the V_{Br} vacancy defect with a density of $\sim 10^{13}$ cm^{-2}, in addition to at least one more type of defect with a much lower density of $\sim 3 \times 10^{11}$ cm^{-2}. In low-temperature photoluminescence (PL), we identify a spectral doublet that shows power saturation that we ascribe to emission from defects. This defect emission is magnetically correlated with the bulk magnetic order but shows up to ~ 100 times smaller energy changes compared with the bulk excitons, which reflects the small but finite interlayer delocalization of the defect wave function when changing from an AFM to ferromagnetic (FM) order. Most strikingly, we observe sharp crossover behavior with the defect PL to reveal a drastic spectral narrowing at T_D that is associated with the emergence of the low-temperature magnetic order. We calculate the electronic structure of the three most prolific point vacancy defects (V_{Cr}, V_S and V_{Br}) and, furthermore, determine the impact of their presence on the local Heisenberg exchange coupling. Our experimental and theoretical results suggest that the low-temperature magnetic order originates from the collective FM alignment of defects. The defects are either the origin of the phase or "sense" this phase as optically active spin defects. The main mechanism creating this magnetic order is likely driven by a complex competition of thermal energy
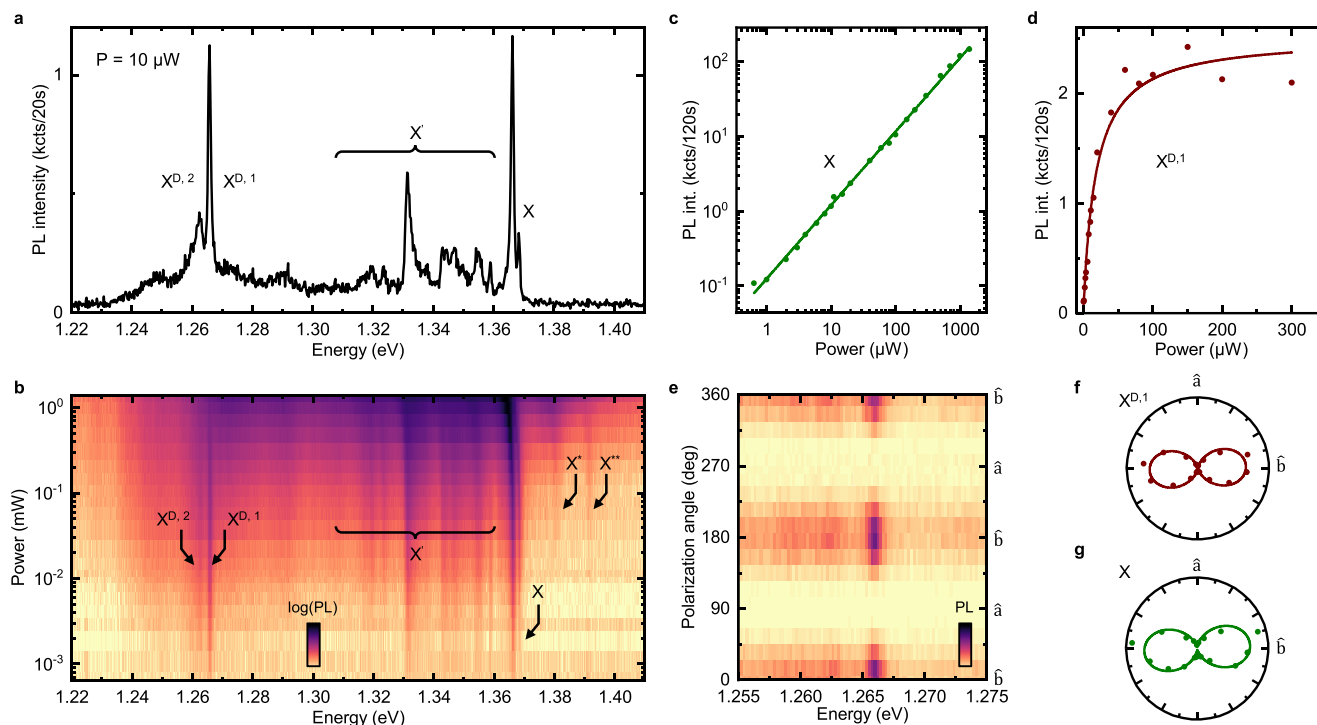
Figure 2. Spectrally narrow defect photoluminescence in CrSBr. (a) Low-temperature (4.2 K) photoluminescence of multilayer CrSBr for an excitation power of 10 μW and a laser energy of 2.384 eV. The 1s exciton X and the defect doublet are highlighted. (b) False color plot of the power dependence of the multilayer CrSBr spectrum. (c) Linear power dependence of the 1s exciton (X). (d) The defect peak shows a clear power saturation behavior with a saturation power of $P_S = 17.99 \pm 2.15$ μW. This represents the saturation power for an ensemble of defects within the interaction volume of the laser spot. (e) Polarization-dependent defect PL shows a strong linear polarization along the b axis and the absence of PL along the a axis. Corresponding polar plots for the defect emission ($X^{D,1}$) and exciton (X) emission are shown in (f) and (g), respectively. An excitation power of 20 μW and an excitation energy of 1.733 eV is used.

k_BT, local and nonlocal exchange interaction, and charge carrier doping. These results overall suggest that strong opportunities exist for exploiting functional defects in CrSBr and vdW magnetic materials more generally and provide a motivation for the controlled generation of magnetic phases by atomic-level defect engineering in vdW magnets with the characteristic of direct optical detection.

RESULTS AND DISCUSSION

Intrinsic Point Vacancy Defects in CrSBr. We first discuss the nature of point defects in CrSBr, whose crystal structure and ground-state magnetic ordering are schematically depicted in Figure 1a. CrSBr is an A-type antiferromagnet with an in-plane FM coupling and a weak interlayer AFM coupling. Measurement of the magnetization of bulk CrSBr (see Figure 1b) shows the easy axis pointing along the b axis with a spin flip transition at $B_{flip} = 0.35$ T, an intermediate magnetic axis along the a axis (1 T), and the hard axis along the c axis (2 T).[29,31] The three most prolific point vacancy defects are V_{Cr}, V_S, and V_{Br}, which are depicted in Figure 1a.

We measure the defect character and density by studying a clean CrSBr surface in STM at room temperature. Figure 1c shows a large-area topographic image of CrSBr. We observe a low density ($\sim 3 \times 10^{11}$ cm^{-2}) of defects D^* that have strong electronic contrast. These defects are not related to the surface but situated below the Br atoms, presumably within the Cr–S matrix, thereby indicating that they originate from the V_S or V_{Cr} vacancy defect or a potentially more complex defect structure. Moreover, from high-resolution topographic images (see Figure 1d) we determine a high top surface concentration

of $\sim 5 \times 10^{12}$ cm^{-2} of V_{Br} that can be clearly distinguished by missing atoms in the periodically arranged Br atoms in the top surface. Their concentration corresponds to a sheet vacancy density of $\sim 10^{13}$ cm^{-2}, which assumes that the top and bottom Br plane both host the same number of V_{Br}. This V_{Br} concentration is almost 2 orders of magnitude higher than the other prevalent defects. The abundance of V_{Br} is also thermodynamically expected from our calculated defect formation energies where $E_{form}^{Br} = 3$ eV is much smaller than $E_{form}^S = 5$ eV and $E_{form}^{Cr} = 7$ eV, respectively. The high density of V_{Br} can potentially explain the commonly observed n-type doping of CrSBr in magneto-transport[31,33,34] with high-room-temperature sheet densities of $\sim 7 \times 10^{13}$ cm^{-2}.[33]

We study the effect of each vacancy on the local electronic environment by performing ab initio calculations of a monolayer CrSBr with the Heyd–Scuseria–Ernzerhof hybrid (HSE) functional for the three most common defects, V_{Cr}, V_S, and V_{Br}, in a $7 \times 7 \times 1$ supercell corresponding to a defect density of $\sim 1.2 \times 10^{13}$ cm^{-2} (see Figure 1e–g). On the basis of these calculations, we expect that the V_{Cr} and V_S can induce four midgap states; we expect only two midgap states for V_{Br}. The corresponding electronic wave functions of the V_{Cr}, V_S, and V_{Br} are shown in Figure 1h,i. The V_{Cr} appears as the most localized in the a–b plane, the V_S is the most delocalized along the b axis, and the V_{Br} is the most delocalized along the a axis, with all defects following the D_{2h} symmetry of CrSBr. We, furthermore, calculate the local change in the magnetic structure to determine the local Heisenberg exchange interaction J (see Figure 1k–m). The V_{Cr} induces a magnetic hole in the lattice with slightly higher exchange energies

compared with the pristine lattice, while the V_{Br} shows the highest local exchange energy. We note for later reference that the local exchange of the V_S is smaller and even negative (AFM) along the a axis, and that, in particular, the V_S defect has a highly anisotropic wave function, with a large extent along the more dispersive b axis.[35]

Spectrally Narrow Defect Emission in Bulk CrSBr. Now that we have established the types and densities of the defects present, we measure their optical properties in multilayer CrSBr. For our PL measurements, we excite the material with a continuous-wave laser at an energy of 2.384 eV with the sample kept at a lattice temperature of 4.2 K. A PL spectrum from a CrSBr flake with a thickness of 36.8 nm (~47 layers) taken with an excitation power of 10 μW reveals a rich optical spectrum (see Figure 2a). The high crystal quality in combination with the preserved 1D character in the bulk provides very clean optical signatures with spectral line widths of only 1 meV.[35] From an excitation power dependence, we can track the evolution of all emission lines (see Figure 2b).

The spectrum shows emission from the 1s exciton (X) and additional resonances at higher energy ($X*$ and $X**$).[35] The fine structure in X is likely from interference effects due to the finite thickness of the flake.[35] The sequence of optical features (X') in the energy window 50 meV below X is of unknown origin and not discussed further here.

While these resonances exhibit a linear power dependence (see, e.g., X in Figure 2c), the doublet peak labeled $X^{D,1}$ and $X^{D,2}$ at ~1.2658 and ~1.2624 eV shows a saturating power dependence (see Figure 2d). This is a clear distinction from bulk exciton emission and an unambiguous signature of emission from defects. The doublet fine structure with an energy splitting of 3.4 meV is layer-independent, unlike the fine structure in the X, and therefore, does not result from interference effects but is of real electronic origin [see the Supporting Information (SI)].

The excitation power dependent emission intensity is well described with $I(X^D) \sim \frac{A \times P}{P + P_{sat}}$ (see Figure 2d). We note that the emission of X^D is not an individual defect but rather the emission from an ensemble of defects within the laser spot. The emission is quenched for a high excitation power throughout all temperatures as expected for defects (see SI Figure 7). Moreover, the defect emission is also strongly linearly polarized along the b axis (see Figure 2e,f), similarly to the excitonic emission (see Figure 2g), which indicates the anisotropic electronic structure. The calculated absorption of the V_S along the b axis is in closest agreement with the measured polarization (see SI).

Electronic Structure of the Luminescent Defect. The relaxation dynamics and carrier pathways for different excitation energies can provide additional insights into the electronic structure of the luminescent defect. We probe the electronic structure of the defect in photoluminescence excitation (PLE) spectroscopy using a spectrally narrow (1 neV) energy-tunable continuous-wave Ti:Sapph laser. In our experiment, we study excitation energies ranging from 1.34 to 1.77 eV. Figure 3a shows a false color map of the PLE measurement. The PL intensity of the X and the X^D shows a similar dependence between 1.5 and 1.77 eV (see also the full energy range in the SI). The increasing PL intensity at 1.77 eV is due to higher energy bands[32,35] while the intensity increase at ~1.55 eV is likely from the high density of states (DOS) at the bulk single-particle band gap (~1.58 eV).[35] More
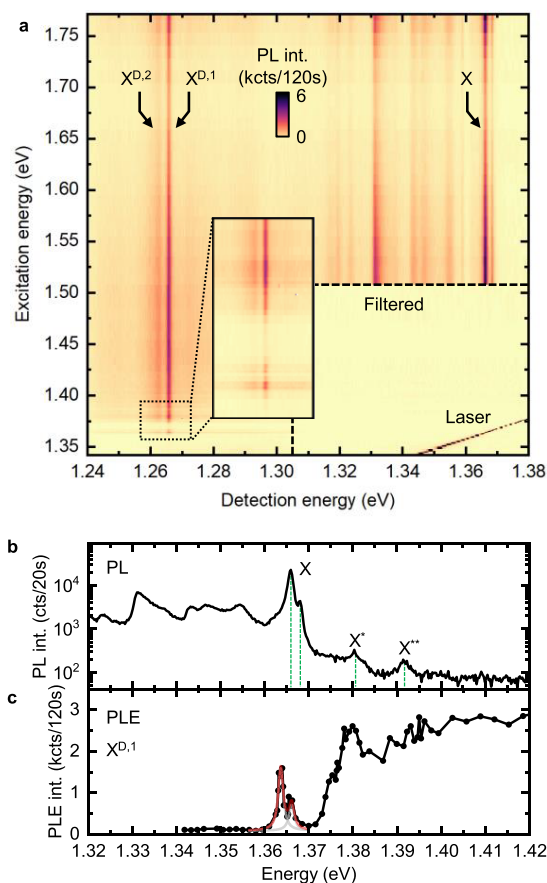

Figure 3. Electronic structure of defect emission in CrSBr. (a) Low-temperature (4.2 K) PLE spectroscopy of multilayer CrSBr. The 1s exciton and defect doublet X^D are indicated by arrows. An excitation power of 20 μW is used. (b) PL spectrum on a semilogarithmic scale highlighting excitonic transitions X, $X*$, and $X**$. (c) Dependence of the defect intensity $X^{D,1}$ on the excitation energy. The resonances in the defect intensity reveal the excitonic structure of CrSBr. The red line is a fit to the excitonic doublet with a line width of 1.2 meV and a splitting of 2.45 meV, which is in excellent agreement with the PL spectrum.

importantly, tuning the laser to the energy window where excitons dominate the material's response at 1.355 eV (see PL in Figure 3b) reveals a clear, fine structure in the PLE of the defect emission $X^{D,1}$ (see Figure 3c and magnified inset in Figure 3a) consisting of a doublet at 1.3659 and 1.3684 eV and an additional peak at 1.381 eV. Direct comparison with the PL spectrum obtained with an excitation energy of 1.7 eV at the same position is in excellent agreement with the X doublet and the $X*$. The third peak (labeled $X**$) observed in PL is not fully resolved in the PLE, likely because of the smaller signal. The clearly resolved electronic and excitonic structure in the defect emission suggests that the defect can be excited efficiently by tuning the laser on resonance with points of high absorption in the electronic structure of CrSBr. The photoexcited electrons and holes can relax and populate the defect level efficiently followed by radiative recombination.

Sensing the Magnetic Order through Optically Active Defects. It is now particularly interesting if the optically active defects embedded in the magnetic environment can be used as a probe of the local magnetic order. We, therefore, measure the defect photoluminescence as we control the magnetic order of
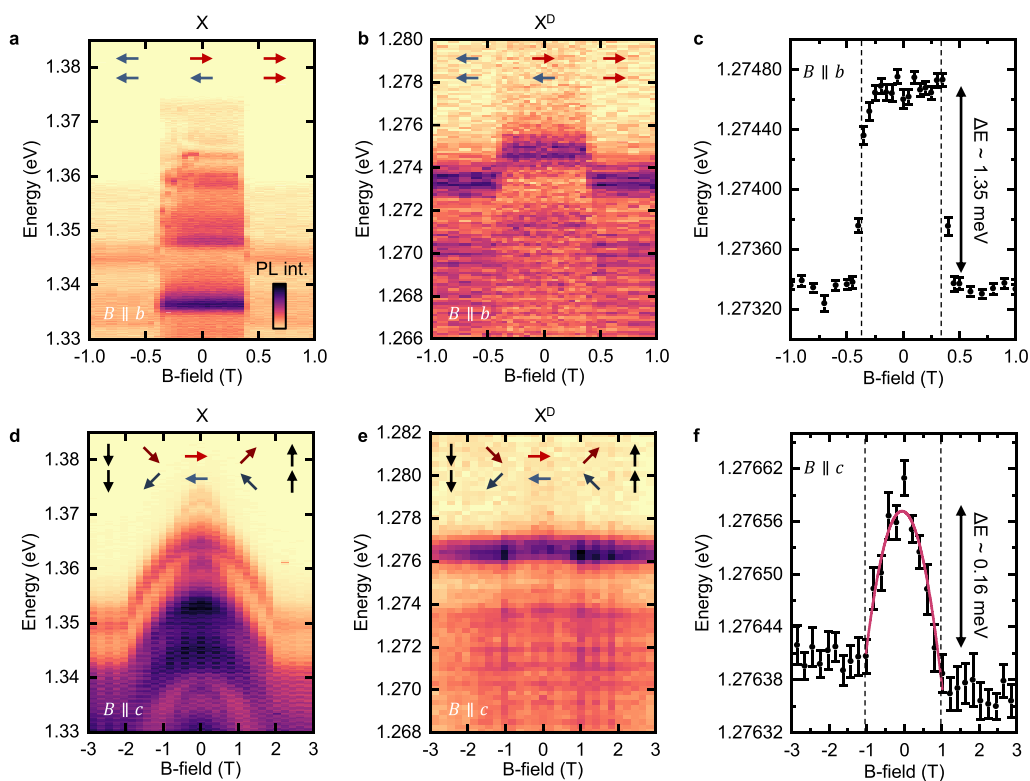
Figure 4. Sensing the magnetic order through optically active defects. (a) Magnetic-field-dependent PL of the excitons in a multilayer CrSBr for the magnetic field B applied parallel to the b axis. The exciton PL shifts when reaching the coercive field at B_{flip} = ~0.35 T because of a spin flip process where the AFM order changes to an FM order. Inset: AFM and FM ordering depicted in the reduced bilayer picture. An excitation power of 100 μW and an excitation energy of 2.33 eV are used. (b) Magnetic-field-dependent PL of the defect emission X^D for the magnetic field B applied parallel to the b axis. The emission shows a sudden red shift at the coercive field of the bulk CrSBr at B_{flip} = ~0.35 T. (c) Corresponding fitted emission energy of $X^{D,1}$ shows a small-energy red shift of 1.35 meV at B_{flip} = ~0.35 T. (d) Magnetic-field-dependent PL of the excitons for the magnetic field B applied parallel to the c axis. The exciton PL continuously shifts until reaching the coercive field at B = ~2 T because of spin canting along the c axis. This changes from an in-plane AFM order to an out-of-plane FM order. Inset: AFM and FM ordering depicted in the reduced bilayer picture. (e) Magnetic-field-dependent PL of the defect emission X^D for the magnetic field B applied parallel to the c axis. The emission continuously red shifts until a field of B = ~1 T. (f) Corresponding emission energy of $X^{D,1}$ shows a small maximum-energy red shift of ~0.16 meV at B = ~1 T. The colored line is a parabolic fit to the data.

the bulk crystal in an external magnetic field. Changes in the emission energy are expected to result from a change in magnetic order.[32]

We begin by applying an external magnetic field along the b axis (see Figure 4). The exciton shows the expected abrupt red shift of ~20 meV when the magnetic field exceeds the spin flip transition field of B_{flip} = 0.35 T along the easy axis (see Figure 4a). This is in agreement with the sudden spin flip transition from AFM to FM order also observed in our magnetization measurements (see Figure 1b). Strikingly, the defect shows a qualitatively similar dependence with an energy red shift at the same critical magnetic field (see Figure 4b). However, the magnitude of the energy shift is ~15 times lower than that of the exciton, with only ~1.35 meV (see Figure 4c). This small energy shift suggests that the wave function of the defect is significantly more localized within the layer but still exhibits a finite extent into the neighboring layer (i.e., a finite carrier tunneling rate τ) when the magnetic order undergoes a transition from AFM to FM.

We now apply the magnetic field along the c axis (see Figure 4d). The exciton reveals a continuous red shift due to the spins canting along the direction of the B field until the saturation field of 2 T is reached. In strong contrast, the defect emission exhibits a very small continuous energy red shift (see Figure

4e,f) of only ~0.16 meV. The energy shift is a factor ~100 times smaller than that of the exciton. Moreover, the energy shift follows a parabolic dependence that agrees with the tunneling probability $\tau \propto B^2$ from second-order perturbation theory considerations.[32] Interestingly, the energy only shifts until reaching a magnetic field of 1 T, which is well below the saturation field of 2 T for the exciton.

The magnitude of the shift is expected to correlate with the wave function delocalization in the FM order.[32] Generally, the sensitivity for energy shifts of the exciton in a magnetic field is due to the admixture of Cr d orbitals with either in-plane or out-of-plane character.[35] The observed difference in energy shift ΔE for the b and c axis of the defect emission is likely due to the different Cr d orbital wave function admixture into the defect bands that are involved in the optical defect transition and the particular geometry of the defect wave function in real space (see Figure 1h–j). We calculate the orbital admixture into the defect bands of the V_{Cr}, V_S, and V_{Br} (see SI). The calculations suggest strong differences in d orbital admixture for the three defects. In particular, the V_S exhibits a strong admixture of Cr d orbitals into its four defect bands. While all four defect bands share some out-of-plane character from d_{z^2} orbitals, the two donor bands close to the conduction band have more in-plane character with $d_{(y^2-x^2)}$, while the two
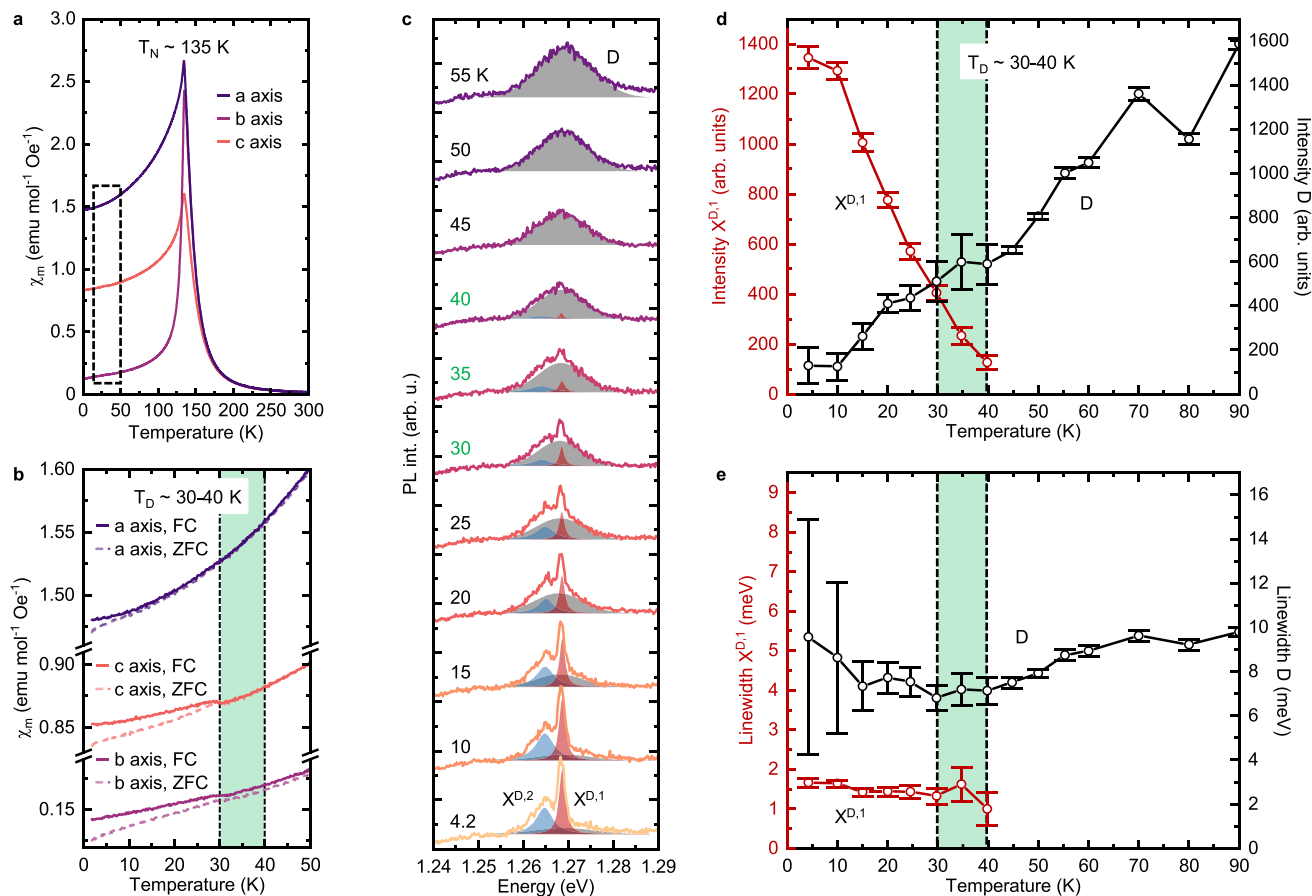
Figure 5. Low-temperature defect magnetic order and optically active defects in CrSBr. (a) Magnetic susceptibility χ_m versus temperature along the a axis, b axis, and the c axis for a CrSBr bulk crystal. Measurements are performed at a magnetic field of 10 mT. (b) Magnification of (a) showing a very weak signature of the low-temperature magnetic order emerging at 30−40 K with a hysteresis behavior that suggests a FM order from field cooling (FC) and zero-field cooling (ZFC). (c) Waterfall representation of the temperature evolution of the defect doublet, $X^{D,1}$ and $X^{D,2}$, PL merging into the D peak. $X^{D,1}$ and $X^{D,2}$ are fitted with Lorentzian lines, and D is fitted with a Gaussian line. An excitation power of 20 μW and an excitation energy of 1.511 eV are used. (d) Temperature-dependent intensity of the $X^{D,1}$ and the D peak. (e) Temperature-dependent line width of $X^{D,1}$ and D.

acceptor bands close to the valence band have out-of-plane character d_{xz}. The anisotropy in the energy shift points toward an anisotropy in the defect wave function in combination with the orbital admixture. In our case, the defect is more sensitive to out-of-plane changes than it is to in-plane changes in magnetic order. Such geometric considerations are of particular interest for the sensing of local magnetic fields. Moreover, defect emission in 2D materials exhibits excitonic character because of the admixture of bulk bands into the defect state. In the future, calculations that include interactions and excitonic effects for defects will be helpful to better understand the excitonic properties of the defects in CrSBr.

Low-Temperature Magnetic Order and Optically Active Defect Emitters. Because we have established that defects in CrSBr are local probes of their magnetic environment, we now focus on the role crystal defects play in the emergence of the defect-induced magnetic order in the temperature range $T_D = 30−40$ K. We are particularly interested in how an ensemble of defects creates a magnetic order, how the defects interact with the magnetic lattice, and also what role interdefect interaction effects have in light of proximity effects and the experimentally measured defect densities.

We begin with studying the correlation of the optically active defects with the low-temperature magnetic order. Therefore, we measure the magnetic susceptibility χ_m by vibrating sample magnetometry (VSM) for field cooling (FC) and zero-field cooling (ZFC) along the three main crystallographic axes (see Figure 5a,b). Our data clearly show the expected cusp of the Neél temperature at $T_N = 135$ K. Moreover, we observe the magnetic order at the characteristic temperature $T_D = 30−40$ K, albeit with a very weak signal amplitude. This signature is universally observed in all crystals at around the same temperature.[31,33,36,37] The weaker signature in χ_m in combination with very narrow photoluminescence line widths and a more intrinsic behavior from scanning tunneling spectroscopy,[35] together, suggest a lower defect concentration in our CrSBr crystals.

We now examine the temperature dependence of the defect emission to track spectral changes in the temperature range of the low-temperature magnetic order (see Figure 5c). Strikingly, upon warming from base temperature ($T = 4.2$ K), the sharp spectral doublet of the defect $X^{D,1}$ and $X^{D,2}$ that exhibits a Lorentzian line shape disappears at $T_D = 30−40$ K that is associated with the low-temperature magnetic order and merges into a peak labeled D with a Gaussian line shape. Throughout the temperature evolution, the intensity of $X^{D,1}$
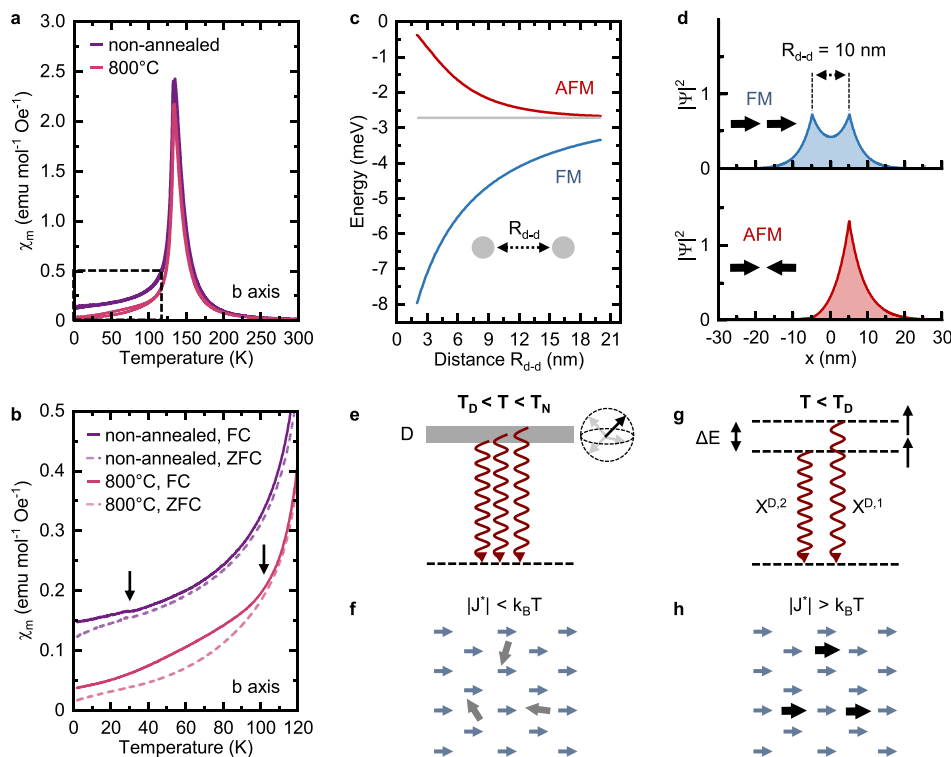
Figure 6. Low-temperature magnetic order from defect−defect interactions. (a) Magnetic susceptibility χ_m versus temperature along the b axis for a nonannealed and for a 24 h at 800 °C annealed CrSBr crystal. Measurements are performed at a magnetic field of 10 mT. T_N remains unchanged. (b) Magnification from (a) showing the onset of the defect magnetic order at 30−40 K for the nonannealed and ∼100 K for the annealed crystal. Field cooling (FC) and zero-field cooling (ZFC) sweeps show the hysteretic behavior suggesting a collective ordering. (c) Bound-state energy for the two-spin aligned state (blue), the single spin aligned state (gray), and the spin antialigned state (red) as a function of distance between two defects R_{d-d}. The FM spin alignment is favorable. (d) Polaron wave functions for different spin configurations for impurity separation $r = 10$ nm and scattering length $a = 5$ nm. The FM spin wave function (blue) is lower in energy compared with the AFM spin wave function (red) since it is able to delocalize more easily. (e) Schematic energy diagram of the uncoupled defect transition for $T_D < T < T_N$ exhibiting a random spin, and as a result, an energy-broadened defect transition D. (f) Schematic illustration of the coupling mechanism of individual defect spins and the magnetic lattice. For a temperature $T_D < T < T_N$, the defect spin is not exchange-coupled to the magnetic lattice because the defect−Cr exchange coupling $|J^*| < k_B T$. (g) The FM alignment of the defect spin with the lattice manifests in a well-defined spin transition that suggests the narrowing of defect emission for $T < T_D$. (h) For $T < T_D$, the defect spin is coupled via Heisenberg exchange to the surrounding Cr atoms due to $|J^*| > k_B T$.

decreases as the intensity of D increases (see Figure 5d). The line width of $X^{D,1}$ is about 1.4 meV and remains unchanged within the error bars throughout this transition (see Figure 5e).

The simultaneous observation of T_D where spectral narrowing occurs and the change in χ_m suggests that the emergence of the low-temperature magnetic order is closely related to the optically active defects.

Low-Temperature Magnetic Order from Defect−Defect Interactions. We further probe the hypothesis of a defect origin of the magnetic order below T_N by increasing the defect concentration in a bulk CrSBr crystal by vacuum annealing at 800 °C for 24 h. The annealed CrSBr maintains its magnetic properties with no visible change in T_N (see Figure 6a). However, the onset of the hysteretic signature below T_N in χ_m, as obtained from FC and ZFC sweeps, is situated at a much higher temperature of ∼100 K (see Figure 6b). Given the strong dependence on the concentration of defects, the sharp crossover temperature in the defect emission (see Figure 5c) in combination with the hysteresis in χ_m (see Figure 5b and Figure 6b) suggests the ordering is driven by defect−defect interactions. Now, we discuss possible origins of the interactions.

There are a few plausible mechanisms that can introduce defect−defect interactions, including direct defect exchange, magnon-mediated defect interactions, or carrier-mediated Ruderman−Kittel−Kasuya−Yosida (RKKY)-type interactions.[38−44] We specifically focus on the carrier-mediated origin here given the strong manifestation of the low-temperature magnetic order in magneto-transport signatures,[31,33,36,37] but additional experiments are required to assess the applicability of the other scenarios, especially coupling to magnons.[45]

We see how carriers can mediate the defect−defect interaction by considering a 1D model featuring a single spin-polarized conduction band electron and two localized spin defects, separated by a distance R_{d-d}.[38,39,43,44] These defect spins then interact with the carrier by a local s−d exchange interaction, with strength K_d. This model is supported by the extreme electronic anisotropy of CrSBr and very light effective electron mass of $m_Y^* = \sim 0.14 m_0$ in the dispersive b axis[35] and the dependence upon doping of the effect observed in magneto-transport.[33]

Within this model, we compare the energies associated with the FM spin state and the AFM spin state of the two defect spins as functions of the defect separation R_{d-d} (see Figure 6c).

Even for a single impurity, when the spin is aligned with the conduction band, a bound state will form, and in the infinitesimally localized contact interaction limit, this bound state energy is $E_1 = -\frac{\hbar^2}{8m \times a^2}$, where a is the (bound-state) scattering length of the potential determined by $1/a = m \times K_d$ (see SI). The various binding energies for the bound states are shown in Figure 6c for the scattering length of a = 5 nm (see scattering length dependence in the SI). Notably, the effect diminishes for a larger scattering length, and our choice of the scattering length is a conservative estimate on the basis of STM topographic images (see Figure 1c,d). Indeed, we see a strong dependence on the distance between the two defects, and notably, we find that while the AFM spin state tends toward essentially the single-defect energy, the FM spin state retains a noticeable lowering of the bound-state energy compared with the single-defect energy, even at large distances. Moreover, a reduced interdefect distance R_{d-d} (higher defect concentration) is expected to result in a larger bound-state energy reflected by a higher critical transition temperature of the defect order. Indeed, this is experimentally observed for the annealed CrSBr with an increase in T_D (see Figure 6a,b).

The interpretation is shown in Figure 6d, where we compute the corresponding wave functions for FM and AFM spin configurations for R_{d-d} = 10 nm. Essentially, every aligned spin can lead to a bound state, but additionally, when there are multiple aligned spins the bound states can hybridize more effectively by sharing their bound carriers, which lead to a nonlinear contribution to the defect spin interactions. While this model offers a simple and compelling explanation for the origin of the low-temperature magnetic order, it clearly requires a more detailed treatment, which we leave to future studies.

Above the critical temperature but below the Néel temperature ($T_D < T < T_N$), the Cr spins are FM-aligned in each layer. In this temperature window, since $k_B T_D > |J^*|$, the spin of the defects are subject to an exchange field but remain unpolarized, as thermal fluctuations overwhelm the exchange and lead to randomly oriented defect spins (see Figure 6e,f). This agrees with broad Gaussian lineshaped emission of the defect D (see Figure 5c). However, when $k_B T_D < |J^*|$, the exchange interaction dominates over thermal disorder and can lead to a net polarization of the defect spins. The sign of J^* then determines whether the defects align with an overall FM (positive) or AFM (negative) order. In our measurement, the alignment of defect spins in the critical temperature range T_D = ∼30−40 K is accompanied by a narrowing of the defect emission with Lorentzian line shape (see Figure 5c). This is likely due to inhomogeneous spin-dependent broadening of the defect energy, which changes from a broad distribution in the disordered phase (see Figure 6e,f) to a narrower distribution in the ordered phase (see Figure 6g,h).

We can qualitatively compare the predictions of this model with the defect densities obtained from our topographic measurements (see Figure 1c,d) in which the interdefect distances were $L_D = \frac{1}{\sqrt{\sigma}}$ = ∼3 nm in the case of V_{Br} and a higher L_D = ∼18 nm for the other defects D^*. Both densities are within the range where sizable interaction effects can be expected.

We finally discuss the possible origin of the defect emission and its relation to the low-temperature magnetic order. Potential scenarios for defect emission include a defect-to-defect transition, conduction band-to-defect transition or defect-to-valence band transition. The defect emission ∼100 meV below X suggests that the likely candidates are a defect-to-defect transition of the V_S or a defect-to-valence band transition of V_{Br} (see Figure 1f,g). Valence or conduction band admixture would result in more excitonic "flavor" of the defect. This would also agree with the defect showing less excitonic character with a more localized electron and hole wave function, also consistent with the magneto-PL and the temperature-independent emission energy. Furthermore, the V_S is in best agreement with the measured emission polarization along the b axis of the defect emission (see Figure 2e,f), as obtained from the calculated absorption (see SI). Moreover, the magnitude of the χ_m signal of the low-temperature magnetic order suggests a high defect density. We observe a high concentration of V_{Br}, with ∼1% of missing atoms and a low concentration of defect D^* with ∼0.05% of missing atoms. The underlying mechanism of the low-temperature magnetic order can be more complex with more than one type of defect involved. We can imagine two potential scenarios: both the optical emission and the low-temperature magnetic order arise exclusively from the V_{Br}, or the magnetic order is from the V_{Br} but sensed by an optically active defect. In general, the wave function anisotropy of V_S along the 1D chains (dispersive b axis) makes the coupling to free carriers that mediate exchange easier (see Figure 1i,l). While several experimental and theoretical results suggest that the V_S is a potential candidate for the defect emission, ascription of the exact origin is, in general, nontrivial. More complex defects like (self-)interstitials or divacancy defects can also be a potential origin of both optical emission and defect order. Moreover, the position of the Fermi level is important for defect emission.[46] At low temperature, CrSBr becomes insulating,[33] which allows optical occupation of vacancy defect donor levels of the V_{Br} and V_S since they are situated closest to the conduction band minimum. Additional experimental work is required to support its unambiguous identification. However, we note that all our results and interpretation are irrespective of the physical nature of the defect, thereby showing only that different point defects can, indeed, have different roles.

CONCLUSION

In conclusion, we experimentally show optically active defects in the CrSBr that sense the local magnetic environment, including a defect-induced magnetic order at low temperature. The optically active defect is either the origin or part of the mechanism that contributes to the low-temperature magnetic order. Our results demonstrate that opportunities can emerge from the coupling of optically active defects with the underlying magnetic order of the matrix. Higher concentrations of defects can be interesting, if considered similarly to dopants or other stoichiometric changes.

Atomic-level defects with the properties we have discussed here can serve as a means to engineer 2D magnetism and, at the same time, to probe the magnetic order via optical read-out. The optical signal and magnetic correlation has strong potential to harness the considerable advantages of optical experiments, such as probing nonequilibrium dynamics of magnetic systems in a simple experimental geometry. Finally, this work also motivates further efforts to explore the coupling of defects with magnetic quasiparticles like magnons.[45]

METHODS AND EXPERIMENTAL

Sample Fabrication. CrSBr bulk crystals were grown by chemical vapor transport.[47] Samples were fabricated by mechanical exfoliation onto SiO_2/Si substrates. Sample thickness was verified by atomic force microscopy, phase contrast, and Raman spectroscopy for thinner flakes.

Photoluminescence Spectroscopy. For the PL measurements, we mounted the sample in closed-cycle helium cryostats (Montana Instruments or AttoDry 800) with a base temperature of 4.2 K. In both setups, measurements were made through the side window using a home-built confocal microscope with a 100×, 0.9 NA objective (Olympus). We excited the sample using a continuous wave (CW) laser at 2.384 eV. The PL was collected confocally after using a long-pass filter. For the polarization-resolved PL, we used a linear polarizer in both excitation and detection and a half-wave plate to rotate the polarization.

Photoluminescence Excitation Spectroscopy. For the PLE measurements, we used a tunable CW Ti:Sapph laser (MSquared Solstis) with a line width of 1 neV. The wavelength was stabilized using feedback from a wavemeter (High Finesse WS8). An excitation power of 20 μW was maintained throughout the measurement well below the saturation power of the defect emission.

Magneto-Optical Spectroscopy. Magnetic field-dependent optical measurements were conducted by mounting a sample of CrSBr bulk flakes on top of a standard SiO_2/Si substrate into a closed-cycle cryostat (AttoDry 2100). The sample was subsequently cooled to temperatures around 1.6 K. Alignment of b or c crystal axes of individual bulk flakes along the axis of the superconducting solenoid magnet, which provided field strengths up to 9 T, was achieved by mounting the sample onto a horizontal sample holder (c axis) or onto a perpendicular sample holder (b axis) and visually aligning. We used a 2.33 eV continuous-wave laser that was fiber-coupled on the input to perform magnetic-field-dependent PL measurements. A second fiber collected the signal from the sample and directed it toward a high-resolution spectrometer attached to a liquid-nitrogen-cooled charge-coupled device camera. The laser excitation power was 100 μW.

Magnetization Measurements. Temperature, field, and angle-dependent magnetic measurements were performed in the temperature range of 1.8−300 K in a Quantum Design Physical Property Measurement System (PPMS) equipped with a 9 T superconducting magnet. Vibrating sample magnetometry (VSM) was employed to characterize the magnetization.

Scanning Tunneling Microscopy. The topographic images were taken at room temperature with a Unisoku UHV-LT four-probe scanning tunnelling microscope operated with a Nanonis controller. The STM was equipped with a scanning electron microscope that allowed precise location of scan locations. The CrSBr bulk crystal was cleaved in vacuum to obtain an adsorbate-free and clean surface, and the data were acquired with both PtIr and W tips.

Ab Inito Calculations. The band structure calculations for the three vacancy defects were calculated using SG15 pseudopotential[48] and the Heyd−Scuseria−Ernzerhof (HSE) hybrid exchange correlation functional.[49] An atomic basis set was used, and spin−orbit coupling was turned on. We used a momentum space k-point sampling of 4 × 3 × 1 for our calculation and a supercell of 7 × 7 × 1 to avoid interaction between defects.

The optical absorption was calculated using the Perdew−Burke−Ernzerhof (PBE) exchange correlation functional[50] and a supercell of 7 × 7 × 1.

Heisenberg Exchange. We investigated the ferromagnetism in monolayer CrSBr in the presence of vacancy defects by calculating the isotropic Heisenberg exchange coupling constant of the nearest neighbor $J_{1,2,3}$ using the Liechtenstein method.[51] For the calculation, we used a 5 × 5 × 1 supercell. For the pristine CrSBr without a defect, we obtained exchange coupling constants of J_1 = 8.21 eV, J_2 = 7.04 eV, and J_3 = 2.28 eV. In our notation, a positive value represents FM coupling, while a negative value corresponds to AFM coupling. Our calculated values are overestimated in comparison with other experimental and theoretical works[52,53] but agree with the expected trend that $J_1 \sim J_2 > J_3$.

ASSOCIATED CONTENT

Data Availability Statement

The data that support the findings of this study and the codes used for data analysis, as well as *ab initio* calculations, are available from the corresponding author on reasonable request.

ⓢ Supporting Information

The Supporting Information is available free of charge at https://pubs.acs.org/doi/10.1021/acsnano.2c07655.

> Scanning tunneling microscopy; power-dependent exciton and defect emission; layer-independent energy splitting of the defect emission; photoluminescence excitation spectroscopy and line width of defect emission; temperature-dependent energy shift; polarization-dependent photoluminesence emission; power-dependence at high excitation power; real-space electronic defect wave function; anisotropy of the electronic structure of defect states; orbital admixture of point vacancy defect states; and theory for defect−carrier interactions (PDF)

AUTHOR INFORMATION

Corresponding Authors

Julian Klein − *Department of Materials Science and Engineering, Massachusetts Institute of Technology, Cambridge, Massachusetts 02139, United States;* ⓞ orcid.org/0000-0002-0873-8224; Email: jpklein@mit.edu

Prineha Narang − *John A. Paulson School of Engineering and Applied Sciences, Harvard University, Cambridge, Massachusetts 02138, United States; College of Letters and Science, UCLA, Los Angeles, California 90095, United States;* ⓞ orcid.org/0000-0003-3956-4594; Email: prineha@ucla.edu

Frances M. Ross − *Department of Materials Science and Engineering, Massachusetts Institute of Technology, Cambridge, Massachusetts 02139, United States;* ⓞ orcid.org/0000-0003-0838-9770; Email: fmross@mit.edu

Authors

Zhigang Song − *John A. Paulson School of Engineering and Applied Sciences, Harvard University, Cambridge, Massachusetts 02138, United States; College of Letters and Science, UCLA, Los Angeles, California 90095, United States*

Benjamin Pingault − *John A. Paulson School of Engineering and Applied Sciences, Harvard University, Cambridge, Massachusetts 02138, United States; QuTech, Delft University of Technology, 2600 GA Delft, The Netherlands*

Florian Dirnberger − *Department of Physics, City College of New York, New York, New York 10031, United States*

Hang Chi − *Francis Bitter Magnet Laboratory, Plasma Science and Fusion Center, Massachusetts Institute of Technology, Cambridge, Massachusetts 02139, United States; U.S. Army CCDC Army Research Laboratory, Adelphi, Maryland 20783, United States;* ⓞ orcid.org/0000-0002-1299-1150

Jonathan B. Curtis − *John A. Paulson School of Engineering and Applied Sciences, Harvard University, Cambridge, Massachusetts 02138, United States; College of Letters and Science, UCLA, Los Angeles, California 90095, United States*

Rami Dana − *Department of Materials Science and Engineering, Massachusetts Institute of Technology, Cambridge, Massachusetts 02139, United States*

Rezlind Bushati − *Department of Physics, City College of New York, New York, New York 10031, United States; Department of Physics, The Graduate Center, City University of New York, New York, New York 10016, United States*

Jiamin Quan − *Department of Electrical and Computer Engineering, The University of Texas at Austin, Austin, Texas 78712, United States; Photonics Initiative, CUNY Advanced Science Research Center, New York, New York 10031, United States; Department of Electrical Engineering, City College of the City University of New York, New York, New York 10031, United States; Physics Program, Graduate Center, City University of New York, New York, New York 10026, United States*

Lukas Dekanovsky − *Department of Inorganic Chemistry, University of Chemistry and Technology Prague, 166 28 Prague 6, Czech Republic*

Zdenek Sofer − *Department of Inorganic Chemistry, University of Chemistry and Technology Prague, 166 28 Prague 6, Czech Republic*

Andrea Alù − *Department of Electrical and Computer Engineering, The University of Texas at Austin, Austin, Texas 78712, United States; Photonics Initiative, CUNY Advanced Science Research Center, New York, New York 10031, United States; Department of Electrical Engineering, City College of the City University of New York, New York, New York 10031, United States; Physics Program, Graduate Center, City University of New York, New York, New York 10026, United States*

Vinod M. Menon − *Department of Physics, City College of New York, New York, New York 10031, United States; Department of Physics, The Graduate Center, City University of New York, New York, New York 10016, United States;* orcid.org/0000-0002-9725-6445

Jagadeesh S. Moodera − *Francis Bitter Magnet Laboratory, Plasma Science and Fusion Center and Department of Physics, Massachusetts Institute of Technology, Cambridge, Massachusetts 02139, United States*

Marko Lončar − *John A. Paulson School of Engineering and Applied Sciences, Harvard University, Cambridge, Massachusetts 02138, United States*

Complete contact information is available at:
https://pubs.acs.org/10.1021/acsnano.2c07655

Author Contributions

J.K. conceived the project and designed the experiments under supervision of F.M.R. and prepared the samples. J.K. and B.P. performed the PL and PLE optical measurements; F.D., R.B., and J.Q. performed magneto-PL measurements; H.C. and J.S.M. collected and analyzed VSM data; R.D. and J.K. performed STM measurements; Z.Sofer and L.D. synthesized CrSBr crystals; J.K. analyzed the experimental data; Z.Song provided ab initio calculations; and J.B.C. modeled the polaron exchange. Work by Z.Song and J.B.C. was supervised by P.N.; V.M.M., A.A., and M.L. discussed results. J.K. wrote the manuscript with input from all coauthors.

Notes

The authors declare no competing financial interest.

REFERENCES

(1) Degen, C.; Reinhard, F.; Cappellaro, P. Quantum sensing. *Rev. Mod. Phys.* **2017**, *89*, 035002.

(2) Casola, F.; van der Sar, T.; Yacoby, A. Probing condensed matter physics with magnetometry based on nitrogen-vacancy centres in diamond. *Nature Reviews Materials* **2018**, *3*, 17088.

(3) Atatüre, M.; Englund, D.; Vamivakas, N.; Lee, S.-Y.; Wrachtrup, J. Material platforms for spin-based photonic quantum technologies. *Nature Reviews Materials* **2018**, *3*, 38−51.

(4) Liu, X.; Hersam, M. C. 2D materials for quantum information science. *Nature Reviews Materials* **2019**, *4*, 669−684.

(5) Bhaskar, M. K.; Riedinger, R.; Machielse, B.; Levonian, D. S.; Nguyen, C. T.; Knall, E. N.; Park, H.; Englund, D.; Loncar, M.; Sukachev, D. D.; et al. Experimental demonstration of memory-enhanced quantum communication. *Nature* **2020**, *580*, 60−64.

(6) Wolfowicz, G.; Heremans, F. J.; Anderson, C. P.; Kanai, S.; Seo, H.; Gali, A.; Galli, G.; Awschalom, D. D. Quantum guidelines for solid-state spin defects. *Nature Reviews Materials* **2021**, *6*, 906−925.

(7) Hermans, S. L. N.; Pompili, M.; Beukers, H. K. C.; Baier, S.; Borregaard, J.; Hanson, R. Qubit teleportation between non-neighboring nodes in a quantum network. *Nature* **2022**, *605*, 663−668.

(8) Philbin, J. P.; Narang, P. Computational materials insights into solid-state multiqubit systems. *PRX Quantum* **2021**, *2*, 030102.

(9) Balasubramanian, G.; Chan, I. Y.; Kolesov, R.; Al-Hmoud, M.; Tisler, J.; Shin, C.; Kim, C.; Wojcik, A.; Hemmer, P. R.; Krueger, A.; et al. Nanoscale imaging magnetometry with diamond spins under ambient conditions. *Nature* **2008**, *455*, 648−651.

(10) Choi, J.; Zhou, H.; Knowles, H. S.; Landig, R.; Choi, S.; Lukin, M. D. Robust dynamic hamiltonian engineering of many-body spin systems. *Physical Review X* **2020**, *10*, 031002.

(11) Bloch, I.; Dalibard, J.; Zwerger, W. Many-body physics with ultracold gases. *Rev. Mod. Phys.* **2008**, *80*, 885−964.

(12) Choi, J.; Zhou, H.; Choi, S.; Landig, R.; Ho, W. W.; Isoya, J.; Jelezko, F.; Onoda, S.; Sumiya, H.; Abanin, D. A. Probing quantum thermalization of a disordered dipolar spin ensemble with discrete time-crystalline order. *Phys. Rev. Lett.* **2019**, *122*, 043603.

(13) Head-Marsden, K.; Flick, J.; Ciccarino, C. J.; Narang, P. Quantum information and algorithms for correlated quantum matter. *Chem. Rev.* **2021**, *121*, 3061−3120.

(14) Randall, J.; Bradley, C. E.; van der Gronden, F. V.; Galicia, A.; Abobeih, M. H.; Markham, M.; Twitchen, D. J.; Machado, F.; Yao, N. Y.; Taminiau, T. H. Many-body−localized discrete time crystal with a programmable spin-based quantum simulator. *Science* **2021**, *374*, 1474−1478.

(15) Peng, P.; Yin, C.; Huang, X.; Ramanathan, C.; Cappellaro, P. Floquet prethermalization in dipolar spin chains. *Nat. Phys.* **2021**, *17*, 444−447.

(16) Kennes, D. M.; Claassen, M.; Xian, L.; Georges, A.; Millis, A. J.; Hone, J.; Dean, C. R.; Basov, D. N.; Pasupathy, A. N.; Rubio, A. Moiré heterostructures as a condensed-matter quantum simulator. *Nat. Phys.* **2021**, *17*, 155−163.

(17) Gottscholl, A.; Diez, M.; Soltamov, V.; Kasper, C.; Sperlich, A.; Kianinia, M.; Bradac, C.; Aharonovich, I.; Dyakonov, V. Room temperature coherent control of spin defects in hexagonal boron nitride. *Science Advances* **2021**, *7*, eabf3630.

(18) de Vasconcellos, S. M.; Wigger, D.; Wurstbauer, U.; Holleitner, A. W.; Bratschitsch, R.; Kuhn, T. Single-photon emitters in layered van der waals materials. *Physica Status Solidi (b)* **2022**, *259*, 2100566.

(19) Klein, J.; Lorke, M.; Florian, M.; Sigger, F.; Sigl, L.; Rey, S.; Wierzbowski, J.; Cerne, J.; Muller, K.; Mitterreiter, E. Site-selectively generated photon emitters in monolayer MoS$_2$ via local helium ion irradiation. *Nat. Commun.* **2019**, *10*, 2755.

(20) Fournier, C.; Plaud, A.; Roux, S.; Pierret, A.; Rosticher, M.; Watanabe, K.; Taniguchi, T.; Buil, S.; Quelin, X.; Barjon, J. Position-controlled quantum emitters with reproducible emission wavelength in hexagonal boron nitride. *Nat. Commun.* **2021**, *12*, 3779.

(21) Branny, A.; Kumar, S.; Proux, R.; Gerardot, B. D. Deterministic strain-induced arrays of quantum emitters in a two-dimensional semiconductor. *Nat. Commun.* **2017**, *8*, 15053.

(22) Palacios-Berraquero, C.; Kara, D. M.; Montblanch, A. R.-P.; Barbone, M.; Latawiec, P.; Yoon, D.; Ott, A. K.; Loncar, M.; Ferrari, A. C.; Atature, M. Large-scale quantum-emitter arrays in atomically thin semiconductors. *Nat. Commun.* **2017**, *8*, 15093.

(23) Klein, J.; Sigl, L.; Gyger, S.; Barthelmi, K.; Florian, M.; Rey, S.; Taniguchi, T.; Watanabe, K.; Jahnke, F.; Kastl, C.; et al. Engineering the luminescence and generation of individual defect emitters in atomically thin MoS$_2$. *ACS Photonics* **2021**, *8*, 669−677.

(24) Lu, X.; Fei, R.; Zhu, L.; Yang, L. Meron-like topological spin defects in monolayer CrCl$_3$. *Nat. Commun.* **2020**, *11*, 4724.

(25) Gu, P.; Tan, Q.; Wan, Y.; Li, Z.; Peng, Y.; Lai, J.; Ma, J.; Yao, X.; Yang, S.; Yuan, K.; et al. Photoluminescent quantum interference in a van der Waals magnet preserved by symmetry breaking. *ACS Nano* **2020**, *14*, 1003−1010.

(26) Huang, B.; Clark, G.; Navarro-Moratalla, E.; Klein, D. R.; Cheng, R.; Seyler, K. L.; Zhong, D.; Schmidgall, E.; McGuire, M. A.; Cobden, D. H.; et al. Layer-dependent ferromagnetism in a van der Waals crystal down to the monolayer limit. *Nature* **2017**, *546*, 270−273.

(27) Zhang, Y.; Lu, H.; Zhu, X.; Tan, S.; Feng, W.; Liu, Q.; Zhang, W.; Chen, Q.; Liu, Y.; Luo, X. Emergence of Kondo lattice behavior in a van der Waals itinerant ferromagnet, Fe$_3$GeTe$_2$. *Science Advances* **2018**, *4*, eaao6791.

(28) Katscher, H.; Hahn, H. Über Chalkogenidhalogenide des dreiwertigen Chroms. *Die Naturwissenschaften* **1966**, *53*, 360−361.

(29) Göser, O.; Paul, W.; Kahle, H. Magnetic properties of CrSBr. *J. Magn. Magn. Mater.* **1990**, *92*, 129−136.

(30) Beck, J. Über Chalkogenidhalogenide des Chroms Synthese, Kristallstruktur und Magnetismus von Chromsulfidbromid, CrSBr. *Zeitschrift für anorganische und allgemeine Chemie* **1990**, *585*, 157−167.

(31) Telford, E. J.; Dismukes, A. H.; Lee, K.; Cheng, M.; Wieteska, A.; Bartholomew, A. K.; Chen, Y.-S.; Xu, X.; Pasupathy, A. N.; Zhu, X.; et al. Layered antiferromagnetism induces large negative magnetoresistance in the van der Waals semiconductor CrSBr. *Adv. Mater.* **2020**, *32*, 2003240.

(32) Wilson, N. P.; Lee, K.; Cenker, J.; Xie, K.; Dismukes, A. H.; Telford, E. J.; Fonseca, J.; Sivakumar, S.; Dean, C.; Cao, T.; et al. Interlayer electronic coupling on demand in a 2D magnetic semiconductor. *Nat. Mater.* **2021**, *20*, 1657−1662.

(33) Telford, E. J.; Dismukes, A. H.; Dudley, R. L.; Wiscons, R. A.; Lee, K.; Chica, D. G.; Ziebel, M. E.; Han, M.-G.; Yu, J.; Shabani, S.; et al. Coupling between magnetic order and charge transport in a two-dimensional magnetic semiconductor. *Nat. Mater.* **2022**, *21*, 754−760.

(34) Wu, F.; Gutierrez-Lezama, I.; Lopez-Paz, S. A.; Gibertini, M.; Watanabe, K.; Taniguchi, T.; von Rohr, F. O.; Ubrig, N.; Morpurgo, A. F. Quasi-1D electronic transport in a 2D magnetic semiconductor. *Adv. Mater.* **2022**, *34*, 2109759.

(35) Klein, J.; Pingault, B.; Florian, M.; Heißenbüttel, M.; Steinhoff, A.; Song, Z.; Torres, K.; Dirnberger, F.; Curtis, J. B.; Deilmann, T., et al.The bulk van der waals layered magnet CrSBr is a quasi-1D quantum material. *arXiv*, May 26, 2022, 2205.13456, ver. 1..

(36) López-Paz, S. A.; Guguchia, Z.; Pomjakushin, V. Y.; Witteveen, C.; Cervellino, A.; Luetkens, H.; Casati, N.; Morpurgo, A. F.; von Rohr, F. O. Dynamic magnetic crossover at the origin of the hidden-order in van der Waals antiferromagnet CrSBr. *Nat. Commun.* **2022**, *13*, 4745.

(37) Boix-Constant, C.; Manas-Valero, S.; Ruiz, A. M.; Rybakov, A.; Konieczny, K. A.; Pillet, S.; Baldovi, J. J.; Coronado, E. Probing the spin dimensionality in single-layer CrSBr van der Waals hetero-structures by magneto-transport measurements. *Advanced Materials* **2022**, *34* (41), 2204940.

(38) Kaminski, A.; Sarma, S. D. Polaron percolation in diluted magnetic semiconductors. *Phys. Rev. Lett.* **2002**, *88*, 247202.

(39) Durst, A. C.; Bhatt, R. N.; Wolff, P. A. Bound magnetic polaron interactions in insulating doped diluted magnetic semiconductors. *Phys. Rev. B* **2002**, *65*, 235205.

(40) Calderón, M.; Sarma, S. D. Theory of carrier mediated ferromagnetism in dilute magnetic oxides. *Annals of Physics* **2007**, *322*, 2618−2634.

(41) Priour, D. J.; Sarma, S. D. Phase diagram of the disordered RKKY model in dilute magnetic semiconductors. *Phys. Rev. Lett.* **2006**, *97*, 127201.

(42) Tang, G.; Nolting, W. Carrier-induced ferromagnetism in diluted local-moment systems. *Phys. Rev. B* **2007**, *75*, 024426.

(43) Liu, L.; Liu, J. T. C. Theory of the bound magnetic polaron in antiferromagnetic semiconductors. *Phys. Rev. B* **1986**, *33*, 1797−1803.

(44) Bednarski, H.; Spałek, J. Bound-magnetic-polaron molecule in diluted magnetic semiconductors. *J. Phys.: Condens. Matter* **2012**, *24*, 235801.

(45) Bae, Y. J.; Wang, J.; Scheie, A.; Xu, J.; Chica, D. G.; Diederich, G. M.; Cenker, J.; Ziebel, M. E.; Bai, Y.; Ren, H.; et al. Exciton-coupled coherent magnons in a 2D semiconductor. *Nature* **2022**, *609*, 282−286.

(46) Hotger, A.; Klein, J.; Barthelmi, K.; Sigl, L.; Sigger, F.; Manner, W.; Gyger, S.; Florian, M.; Lorke, M.; Jahnke, F.; et al. Gate-switchable arrays of quantum light emitters in contacted monolayer MoS$_2$ van der Waals heterodevices. *Nano Lett.* **2021**, *21*, 1040−1046.

(47) Klein, J.; Pham, T.; Thomsen, J. D.; Curtis, J. B.; Denneulin, T.; Lorke, M.; Florian, M.; Steinhoff, A.; Wiscons, R. A.; Luxa, J. Control of structure and spin texture in the van der waals layered magnet CrSBr. *Nat. Commun.* **2022**, *13*, 5420.

(48) Schlipf, M.; Gygi, F. Optimization algorithm for the generation of ONCV pseudopotentials. *Comput. Phys. Commun.* **2015**, *196*, 36−44.

(49) Heyd, J.; Scuseria, G. E. Efficient hybrid density functional calculations in solids: Assessment of the heyd−scuseria−ernzerhof screened coulomb hybrid functional. *J. Chem. Phys.* **2004**, *121*, 1187−1192.

(50) Perdew, J. P.; Burke, K.; Ernzerhof, M. Generalized gradient approximation made simple. *Phys. Rev. Lett.* **1996**, *77*, 3865−3868.

(51) Terasawa, A.; Matsumoto, M.; Ozaki, T.; Gohda, Y. Efficient algorithm based on Liechtenstein method for computing exchange coupling constants using localized basis set. *J. Phys. Soc. Jpn.* **2019**, *88*, 114706.

(52) Wang, H.; Qi, J.; Qian, X. Electrically tunable high curie temperature two-dimensional ferromagnetism in van der Waals layered crystals. *Appl. Phys. Lett.* **2020**, *117*, 083102.

(53) Scheie, A.; Ziebel, M.; Chica, D. G.; Bae, Y. J.; Wang, X.; Kolesnikov, A. I.; Zhu, X.; Roy, X. Spin waves and magnetic exchange hamiltonian in CrSBr. *Advanced Science* **2022**, *9*, 2202467.

📖 Recommended by ACS

The Bulk van der Waals Layered Magnet CrSBr is a Quasi-1D Material

Julian Klein, Frances M. Ross, *et al.*

MARCH 16, 2023
ACS NANO   READ ☑

Ultrafast Optomechanical Strain in Layered GeS

Duan Luo, Aaron M. Lindenberg, *et al.*

MARCH 10, 2023
NANO LETTERS   READ ☑

Colloidal Ternary Telluride Quantum Dots for Tunable Phase Change Optics in the Visible and Near-Infrared

Dhananjeya Kumaar, Maksym Yarema, *et al.*

MARCH 27, 2023
ACS NANO   READ ☑

Interlayer Exciton–Phonon Bound State in Bi$_2$Se$_3$/Monolayer WS$_2$ van der Waals Heterostructures

Zachariah Hennighausen, Berend T. Jonker, *et al.*

JANUARY 16, 2023
ACS NANO   READ ☑

Get More Suggestions >